Available online at www.sciencedirect.com

SCIENCE DIRECT®

Thermochimica Acta 419 (2004) 239–246

thermochimica acta

www.elsevier.com/locate/tca

Examination of thermal properties by scanning thermal microscopy in ultrafine-grained pure titanium surface layer produced by surface mechanical attrition treatment

F.A. Guo[a], K.Y. Zhu[b], N. Trannoy[a,*], J. Lu[b]

[a] *Unité de Thermique et d'Analyse Physique, Laboratoire d'Energétique et d'Optique, Université de Reims, BP 1039, 51687 Reims Cedex 2, France*
[b] *LASMIS, Université de Technologie de Troyes, 12 Rue Marie Curie, 10010 Troyes, France*

Received 3 October 2003; received in revised form 26 February 2004; accepted 27 February 2004

Abstract

Ultrafine-grained pure titanium surface layer produced by surface mechanical attrition treatment (SMAT) was systematically studied by scanning thermal microscopy (SThM) that allows thermal conductivity to be mapped down to the submicrometer scale. It is found that the microstructures obtained by SMAT show different thermal conductivities that strongly depend on the grain size: the thermal conductivity of the nanostructured surface layer decreases substantially if compared with that of the coarse-grained matrix of the sample. A theoretical approach, based on this investigation, was used to calculate the heat flows from the probe tip to the sample and then estimate the thermal conductivities at different scanning locations. Experimental results and theoretical calculation demonstrate that the SThM analyses can be used as a powerful tool for the thermal property and microstructure analysis of ultrafine-grained microstructures.

Keywords: Ultrafine-grained microstructure; Titanium; Surface mechanical attrition treatment; Scanning thermal microscopy; Thermal conductivity

1. Introduction

Over the last decade, ultrafine-grained materials have attracted considerable scientific interest due to its small grain size and large amount of interfaces. Many studies have shown that a number of properties in these materials are fundamentally different from, and often superior to, those of the conventional polycrystalline materials [1–3].

SMAT is a recently developed technique that can produce various ultrafine-grained structures in the surface layer of bulk material by imposing intense plastic deformation into metals and alloys [4]. Using this processing, different microstructures from nanometer-sized grains to submicrometer-sized and micrometer-sized crystallites within the deformed layer can be obtained. This technique has been successfully applied in achieving surface nanocrystallization in a variety of materials including pure metals and alloys, such as iron [5,6], aluminium [7,8], and stainless steel [9], etc. This kind of surface nanocrystallization would greatly enhance surface properties without changing the chemical composition of the materials.

Efficient utilization of ultrafine-grained materials requires a good understanding of their thermophysical properties. It is known that the heat transport properties of polycrystalline materials are strongly affected by their microstructural features [10,11]. Therefore, obtaining clear information on thermal properties can provide vital information on the intrinsic microstructural characteristics of the ultrafine-grained materials. Obviously, the measurements and investigations of their thermophysical properties are of significance not only for fundamental research but also for applications of this kind of materials.

Invention of the scanning thermal microscopy (SThM) has allowed us to investigate surface thermal properties even down to micrometer or submicrometer spatial resolution. The SThM is based on an atomic force microscopy (AFM), but uses a specialized thermal probe instead of conventional SiN_x tip of the AFM. The SThM is developed to give simultaneously topography image and thermal property image of material surface. In SThM, the interaction between probe

---

[*] Corresponding author. Tel.: +33-3-26-91-33-92; fax: +33-3-26-91-32-50.
E-mail address: nathalie.trannoy@univ-reims.fr (N. Trannoy).

0040-6031/$ – see front matter © 2004 Elsevier B.V. All rights reserved.
doi:10.1016/j.tca.2004.02.018

tip and sample is based on the heat flow. Therefore, differences in temperature or thermal conductivity constitute the imaging contrast.

The SThM has many potential applications, one of them is to study local variations in surface thermal properties. Zhou et al. studied the laser-induced deposition of palladium lines on glass from palladium acetate by means of the thermal contrast variation in thermal conductivity images [12]; Fiege et al. carried out the failure analysis of integrated device by SThM analysis [13]; Ruiz et al. determined the absolute thermal conductivity values of a diamond-like nanocomposite film by calibrating a SThM probe tip [14]; and Buzin et al. [15], Fiege et al. [16,17] carried out the quantitative thermal analyses using 3ω technique. Many interesting results have been obtained from these studies. However, the results obtained by the quantitative analyses have been frequently questioned [18], because the quantitative measurement of the heat is quite complicated. Up-to-date, no work dealt with the analysis of the thermal properties of ultrafine-grained microstructures using SThM technique.

In this paper, the authors combined the SThM and microstructural analysis to study the thermal properties of an ultrafine-grained pure titanium surface layer produced by SMAT. A SThM in the direct current (dc) mode was used to map the thermal conductivity images on the cross-sectional surface of the treated sample. Under the same scanning conditions, the heat flows at different scanning locations were calculated and used to interpret the effects of microstructural features on the thermal conductivities, and then estimate the thermal conductivities at different microstructure regions.

2. Experimental details and theoretical approach

2.1. Sample preparation

A pure titanium plate (10 m × 100 m × 100 m in size) with a purity of 99.95 wt.% was subjected to SMAT in order to achieve an ultrafine-grained surface layer. The set-up and procedures of the SMAT were described in a previous paper [6]. The principle of the SMAT is based on the vibration of spherical shots. During the treatment, repeated multidirectional peening at high strain rates onto sample surface leads to severe plastic deformation in the surface layer and thereby refines the surface microstructure. The main parameters of the SMAT process were chosen as follows: the vibration frequency driven by an ultrasonic generator is 20 kHz, the shot diameter is 3 mm, and the samples used in this work were treated in vacuum for 30 min at room temperature. After the treatment, the sample surface is smooth. Positron annihilation spectroscopy experiments revealed that the surface layer of the treated sample is free from porosity.

The specimens used for thermal conductivity analysis were cut from the SMATed sample. The specimens were embedded in a resin and isolated from other conductive materials. The samples were mechanically polished to a mirror in order to avoid the surface influence on the heat conduction, and the polishing was cautiously carried out at a low temperature to avoid the change of the grain size and the structure of the grain boundaries. The polishing process for the tested specimens and the samples used for probe calibration was the same. An optical microscope and a transmission electron microscope (TEM, Philips EM420 with an accelerating voltage of 100 kV) were used to observe the microstructure after SMAT. Thin foils for TEM observations were prepared by means of ion thinning.

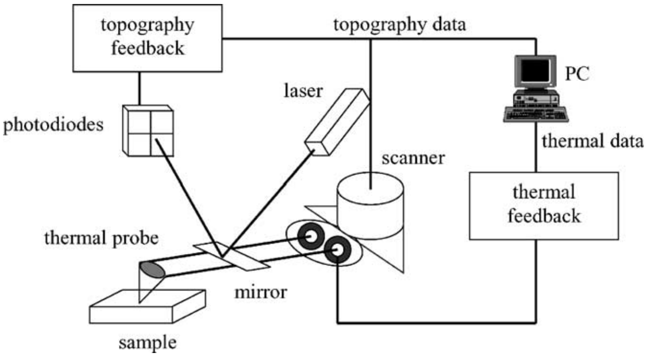

Fig. 1. Schematic diagram of the SThM set-up.

2.2. SThM analysis

For thermal conductivity analysis, a TopoMetrix SThM was employed in which thermal imaging is achieved using a resistive thermal element incorporated at the end of a cantilever that makes it possible to achieve an AFM type feedback. The thermal element consists of a bent filament (5 μm diameter) of platinum/10% rhodium. Fig. 1 depicts the set-up of the SThM used in this work.

In SThM, normally two working modes are available: 'temperature contrast mode' and 'thermal conductivity contrast mode'. In the present work, the 'thermal conductivity contrast mode' was used, in which the thermal probe functions as a resistive heater. The control circuit uses a feedback loop to adjust the voltage applied to the bridge in order to keep the thermal probe at a constant temperature. When the thermal probe is scanned across the sample surface, heat will transfer from the thermal probe to the sample; variations in thermal conductivity across the sample surface will affect the heat flow to the sample. Here, thermal probe is used both as a thermal sensor and a heater.

2.3. Theoretical approach

Fig. 2 depicts the bridge circuit used to maintain the probe tip at a constant temperature. When the probe tip is in the air (far away from the sample surface), the heat flow dissipated into the tip Q_{air} is given by

$$Q_{\mathrm{air}} = \frac{V_{\mathrm{air}}^2}{R_{\mathrm{op}}} \qquad (1)$$

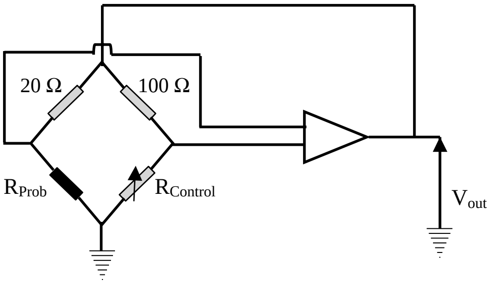

Fig. 2. Schematic diagram of the bridge circuit used to maintain the probe tip at a constant temperature. The R_{control} is chosen to control the operating probe tip temperature.

where V_{air} is the voltage across the probe tip (determined by the bridge circuit) and R_{op} is the probe tip resistance at the operating temperature (T_{op}). R_{op} is determined by the following relation [19]:

$$R_{\text{op}} = R_0[1 + \alpha_{\text{p}}(T_{\text{op}} - T_0)] \tag{2}$$

where R_0 is the probe tip resistance at ambient temperature, α_{p} (=0.00165 $\Omega\,(\Omega\,\text{K})^{-1}$) the resistance coefficient of the platinum/10% rhodium thermoresistive filament and T_0 is the ambient temperature.

When the probe tip is brought in contact with the sample, the total heat dissipated into the probe tip Q_{total} is given by

$$Q_{\text{total}} = \frac{V_{\text{total}}^2}{R_{\text{op}}} \tag{3}$$

V_{total} is obtained from the thermal conductivity images. Therefore, the heat flow going into the sample can be written as

$$Q_{\text{s}} = Q_{\text{total}} - Q_{\text{air}} \tag{4}$$

At an operating temperature, the variations in Q_{s} in different microstructures imply the variation in thermal conductivities with the microstructures.

For a given thermal probe tip, using a series of samples whose thermal conductivities are known, a relation between Q_{s} and thermal conductivity κ_{s} can be obtained under the same scanning conditions, and hence the thermal conductivity of the studied sample can be estimated.

With the help of TEM, we estimated the different microstructure regions in the treated layer. The thermal conductivity scanning was carried out on the cross-section of the sample that includes the treated layer and the matrix. The set-up of the SThM used in this work can not allow us to know the exact distance from the sample surface, so we simply indicated the relative scanning positions at different microstructure regions (see Fig. 3). A series of scanning of dimensions 5 μm × 5 μm were performed from the treated surface layer to the strain-free matrix. In order to avoid the influence of water on heat conduction on the sample surface, the working temperature of the thermal probe was set to be 116.9 °C [20]. The main scanning conditions were chosen as follows: the set point, which controls the force of the probe tip on the sample surface, is 5.5 nA; the PID (proportional gain, integral gain, derivative gain) settings, which control the feedback signals, are 3, 0.2 and 0, respectively. The scan rate is 10 μm/s, and a resolution of 400 lines per scan. For one position indicated in Fig. 3, at least three scans were carried out in the area with the same grain size, and the voltage values for theoretical calculation were taken as the average of these scans.

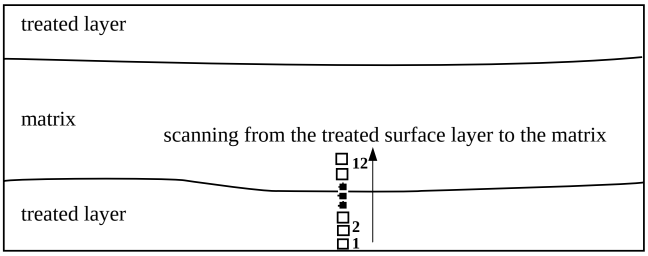

Fig. 3. Schematic diagram of the scanning position from the treated surface layer to the matrix of the sample.

The spatial resolution of SThM is mainly governed by the effective contact area between the probe tip and the sample surface. Despite the fairly large diameter of the platinum/10% rhodium wire (5 μm diameter), the effective contact area is very small (80 nm) [21]. The spatial resolution of the probe used in this work was estimated of 1 μm [22] but 100 nm features had been clearly resolved with this probe [23]. The error of the calculation, which is estimated by the deviation of the measured V_{air} and V_{total}, is about 5%.

3. Results and discussion

3.1. Microstructure

Fig. 4 shows the cross-sectional microstructure of SMATed pure titanium sample observed under an optical microscope. It can be seen that the microstructures in the treated layer change gradually from equiaxed grains of 30–80 μm in diameter in the matrix to ultrafine-grained structures beyond the resolution of the optical microscope in the top layer of the treated surface. TEM observations indicate that the outer surface of the treated layer corresponds to the nanostructured layer with a thickness of about 50–60 μm and the equiaxed nanograins are 50–200 nm in size (see Fig. 5), then the submicrometer-grained and micrometer-sized structures. The thickness of the whole deformed layer is more than 300 μm. These results indicate that SMAT is an effective method to produce ultrafine-grained structures in the surface layer of pure titanium sample.

3.2. Thermal conductivity variation in the deformed layer

Scanning thermal microscopy provides information on thermal conductivity maps not available to conventional AFM and scanning tunneling microscopy (STM). This

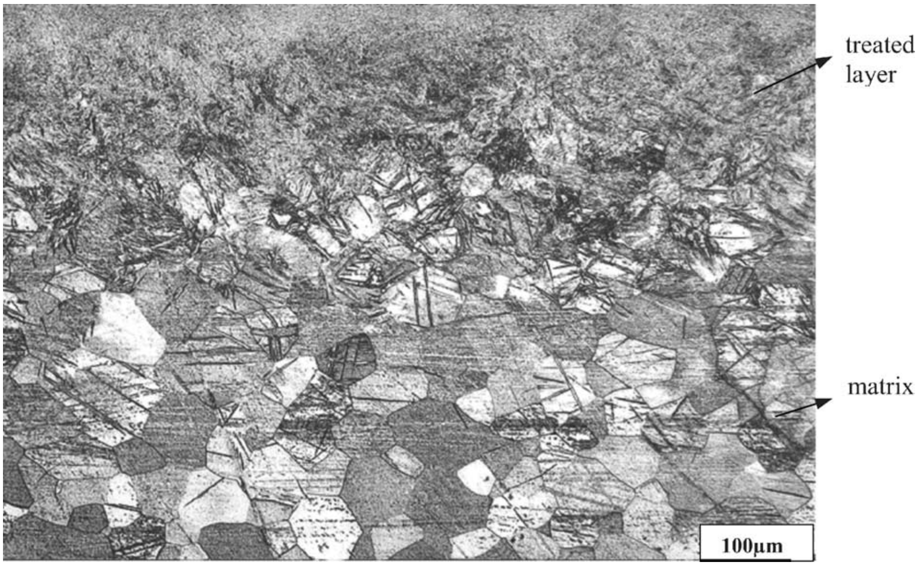

Fig. 4. Optical micrograph on the cross-section of the SMATed pure titanium sample.

offers valuable opportunity to characterize the thermal properties of material surfaces at the submicrometer scale.

In SThM, the thermal image signal is affected by several factors, including sample thermal conductivity, probe-sample temperature differential, and probe-sample effective contact area, etc. In this work, the scanning conditions for each series of scanning were kept identical. Fig. 6 shows a typical topographical image and thermal image obtained in the thermal conductivity contrast mode. In Fig. 6(a), spots 1–3 were induced by the dusts on the sample surface, the corresponding locations in the thermal conductivity image, however, shows opposite contrast due to their low thermal conductivity, as can be seen in Fig. 6(b) indicated by the same numbers.

The mechanically polished sample surface is never perfectly flat, and the end of the probe tip also has some curvature. Therefore, the contrast in Fig. 6(b) can be observed which is mainly due to the relief on the sample surface, leading to variation in probe-sample effective contact area at different contacting points, giving rise to changes in heat flow from the probe tip to the sample, not arising from thermal conductivity difference. In Fig. 6, it can also be observed that the spots and others signals in the thermal conductivity image are larger than those at the corresponding locations in the topographical image. This may be caused by other factors such as submicron surface roughness, mechanical inconsistency which clearly reduce the thermal conduction but have less influence on the topographical signals.

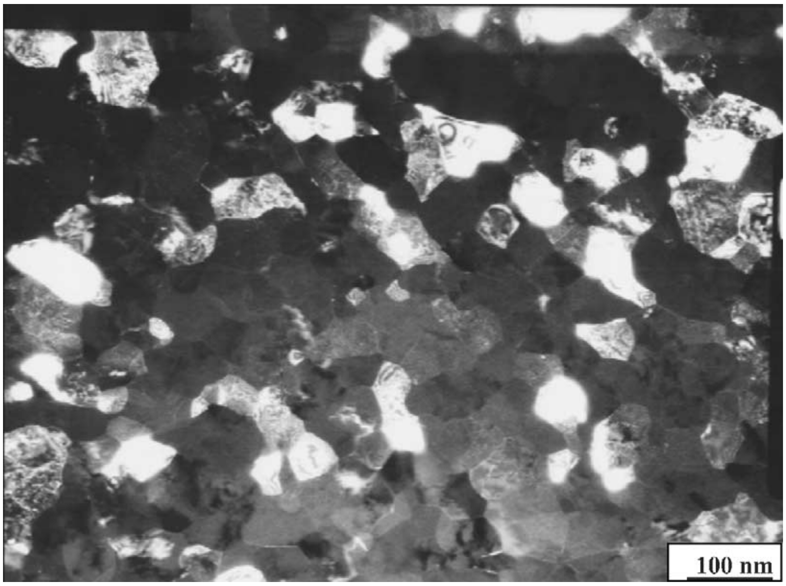

Fig. 5. Dark-field TEM micrograph in the top surface layer (40 μm deep from the treated surface) of the SMATed titanium sample.

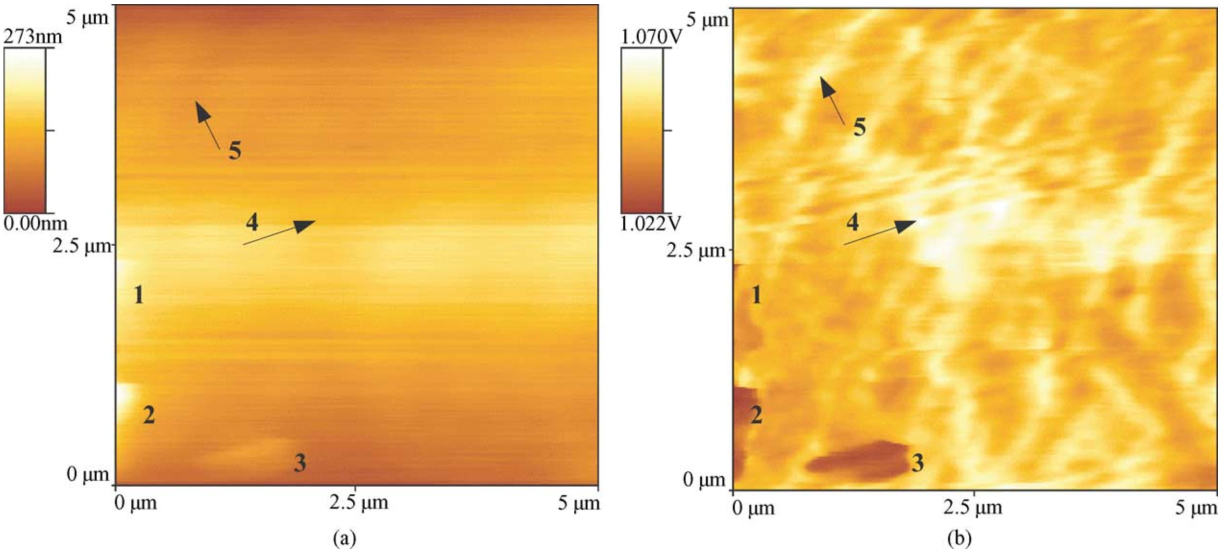

Fig. 6. (a) Topographical image and (b) thermal image of a thermal conductivity scanning.

It should be pointed out that the resolution of the SThM topographical image, which is in correlation with the loop shape of the probe tip wire, is much lower than that of AFM topographical image. In this study, we mainly emphasize the thermal conductivity variation with the microstructural features, and for all the samples used in this study (including the samples used for probe calibration), the polishing process is the same, and we tried to eliminate the dusts on the sample surface before scanning. Therefore, while no significant features can be observed from the topographical images, we do not consider the topography effect on heat conduction. For the theoretical calculation, we used the average values for each thermal image and tried to avoid the influence of the defects on the thermal voltage values, the influence of the contrast on the average thermal values can be neglected.

Fig. 7 shows some typical thermal images of a series of thermal conductivity scanning from the nanostructured surface layer to the matrix (as indicated in Fig. 3) under the same scanning conditions. Fig. 7(a) and (b) were obtained in the nanostructured region, (c) and (d) in the submicrometer and micrometer scaled region, whereas (e) and (f) were obtained in the strain-free matrix. It is interesting to observe that, from the nanostructured surface layer to the matrix, the thermal values on these images increase substantially. While the scanning conditions are the same, and no significant features can be observed from the corresponding topographical images, the thermal value variation obviously shows the variations in the thermal conductivity with the microstructures.

The thermal image is obtained by recording the Wheatstone bridge voltage. It will require more heat flows from the thermal probe to the locations having higher thermal conductivity than to the place with lower thermal conductivity. In order to keep the thermal probe at a constant temperature, the probe requires a higher power compensation over the locations with higher thermal conductivities where therefore appear higher thermal values in the thermal conductivity images.

Fig. 8 presents the variations in Q_s of this series of scanning. It is interesting to observe that, from the nanostructured surface layer to the matrix, Q_s increases obviously, and keeps approximately stable in the matrix. The variations in Q_s imply that, with the refinement of the microstructure, the thermal conductivity decreases substantially.

For polycrystalline materials, several factors can have a significant influence on the thermal conductivity of a sample. Pores, filled with gas of a lower thermal conductivity than the solid phase, help block the heat flow and thus make the material more insulating. Interfaces and grain boundaries, which are crossed by the heat flow path, can also inhibit heat conduction. The impurities and second phases located at the grain boundaries reduce the effective across sectional area of the sample, thereby lower the thermal conductivity.

The SMAT process has some unique advantages compared with the coating and deposition methods for surface nanocrystallization. For example, as there is no change in chemical compositions of the nanostructured surface layer and in the matrix, as well as a gradual variation in the grain size from nanometer-sized grains to coarse-grains, bonding of the nanostructured surface layer with matrix will not be a problem. In addition, the SMATed surface layer is free from porosities and impurities. Therefore, for our studied pure titanium sample, the main factor that strongly affects its thermal conductivity is the grain boundaries.

It is well known that the thermal conduction in solids includes electron conduction and phonon conduction, and the thermal conductivity, κ_s, is normally described by following equation:

$$\kappa_\mathrm{s} = \kappa_\mathrm{phonon} + \kappa_\mathrm{electron} \tag{5}$$

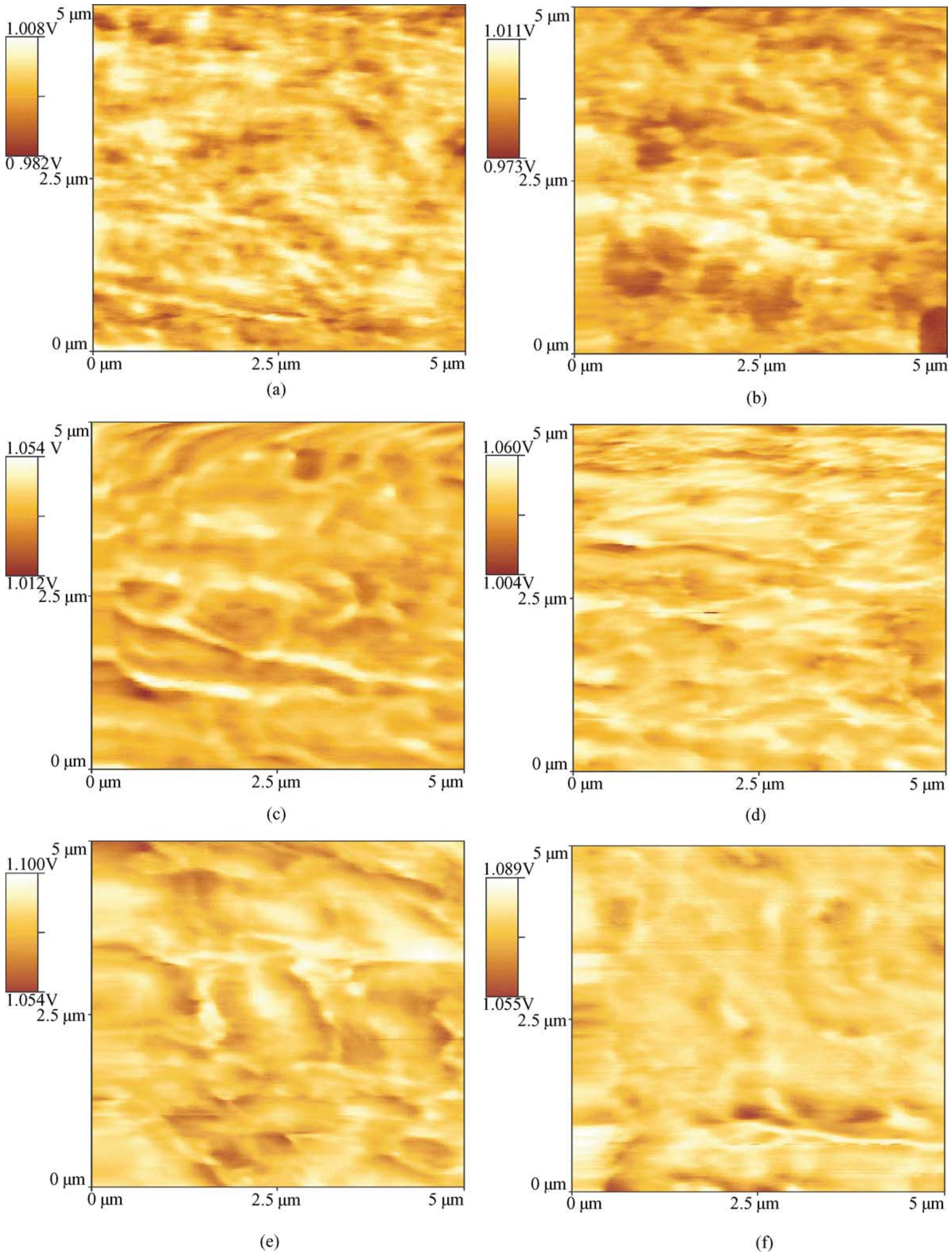

Fig. 7. Some thermal conductivity images of a series of scanning at different locations from the treated surface layer to the matrix as indicated in Fig. 3.

which is the sum of the contributions by phonon (κ_{phonon}) and electron (κ_{electron}) conduction. In general, in pure metals, the main contribution to thermal conductivity comes from electrons [24]. The thermal conductivity of materials is related to the conductive electron density n and the mean free path l of electrons by the following formula [24]:

$$\kappa_s = \frac{\pi^2 k^2 T n l}{3 m v_e} \tag{6}$$

Here κ is the Boltzmann constant, T the temperature, n the effective electron density in a microstructure, m the mass of the conductive electron, and v_e is the Fermi velocity.

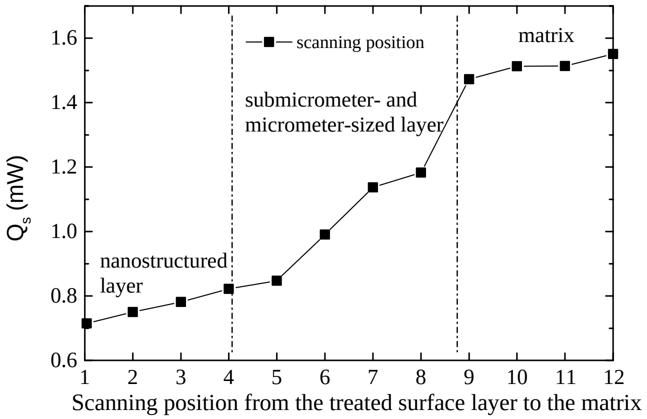

Fig. 8. Variation in the heat flow going into the sample while scanning from the nanostructured surface layer to the matrix as indicated in Fig. 3.

The decrease in thermal conductivity with the reduction of grain size would be mainly due to the decrease of the effective electron density n in the microstructure; since n decreases with the reduction of grain size d by the following relation [25]:

$$n = n_\mathrm{b} T^{*(1/d)} \tag{7}$$

Here T^* (<1) is the transmission coefficient of electron through a potential barrier, and n_b is the conductive electron density in single crystal without boundaries.

With the decrease in the grain size, the reduction of the thermal conductivity of the ultrafine-grained microstructure is also related to the phonon scattering at grain boundaries. Small grain size with large volume fraction of interfaces within which a large amount of defects as well as a high random atomic arrangement may exist, would strongly lead to phonon scattering at the grain boundaries.

In addition, attention should also be paid to the influence of internal defects on the reduction of thermal conductivity. Microscopic evidence indicates that, in the treated layers, there exist not only numerous non-equilibrium grain boundaries, but a high dislocation density and a large value of residual stresses as well [26]. These residual stresses and dislocations can act as both phonon and electron scatterers and thereby reduce the thermal conductivity of the microstructure [27].

3.3. Thermal conductivity estimation

For the thermal conductivity estimation, we calibrated the thermal probe used in this work. A series of materials with known thermal conductivities were used. Fig. 9 shows the relation between Q_S and κ_S for these materials. It can be seen that two segmental lines were obtained by linear fit processing: for the materials with lower thermal conductivities (less than 57 W (m K)$^{-1}$), the relation between Q_S and κ_S is $Q_\mathrm{S} = 0.6905 + 0.0304\kappa_\mathrm{S}$; and for the materials with higher thermal conductivities, the relation is: $Q_\mathrm{S} = 1.2170 + 0.0049\kappa_\mathrm{S}$.

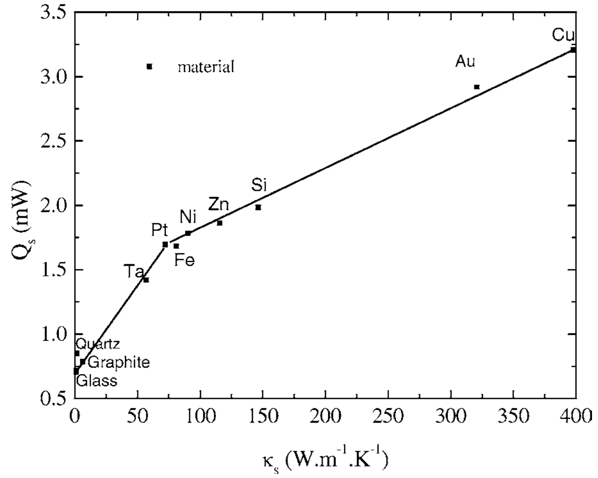

Fig. 9. Heat flow Q_S as a function of κ_S for some materials with known thermal conductivities. The solid line is a least-squares fitting line.

In order to evaluate κ_S of the tested sample, Q_S was calculated at each scanning location under the same scanning conditions as those for the probe calibration. As mentioned above, for Q_S calculation, the average image voltage values were obtained from the thermal conductivity images. The thermal conductivity of coarse-grained pure titanium is about 20 W (m K)$^{-1}$ [28], so the relation $Q_\mathrm{S} = 0.6905 + 0.0304\kappa_\mathrm{S}$ was used.

The thermal conductivity of the matrix (position 12 indicated in Fig. 3) estimated by this method is about 24.6 W (m K)$^{-1}$, and that of the nanostructured layer (position 1 indicated in Fig. 3) is about 5.2 W (m K)$^{-1}$. The thermal conductivity of the coarse-grained matrix obtained in this work is a little higher than that of the coarse-grained pure titanium (about 20 W (m K)$^{-1}$) [28].

These results demonstrate that SThM is a possible method to estimate the thermal conductivities of the ultrafine-grained microstructures and the bulk material with a simple sample preparation. However, there are some drawbacks in this work: (1) the recalibration is necessary if the probe or operating conditions are changed; (2) as discussed above, the thermal voltage values are affected by topographical factors, such as microstructure defects, atom diffusion, grain boundary features. These factors influence the thermal voltage values and thermal imaging. It is easy to understand, but difficult to separate the thermal data from the topographical data in this case. Further, work should be taken in order to obtain the precise values of the thermal image signal. Furthermore, other method should be developed in order to verify the results obtained in this work.

4. Conclusions

Ultrafine-grained structures were produced in the surface layer of a pure titanium plate by surface mechanical attrition treatment. The SThM analyses demonstrate that the thermal conductivity of the ultrafine-grained structures decreases obviously as compared with that of the coarse-grained counterpart. The estimation of the thermal conductivity indicates that SThM is a possible method to estimate the thermal conductivities of the ultrafine-grained microstructures and the bulk material with a simple sample preparation. However, further work should be taken in order to obtain the precise values of the thermal image signal.

Acknowledgements

This work is financially supported by French Ministry of Research and the Regional Council of Champagne-Ardenne France (Grant 2001882, CPER EN2040).

References

[1] H. Gleiter, Prog. Mater. Sci. 33 (1989) 223–315.

[2] V.G. Gryazonov, L.I. Trusov, Prog. Mater. Sci. 37 (1993) 289–401.

[3] K. Lu, Mater. Sci. Eng. Rev. R 16 (1996) 161–221.

[4] J. Lu, Residual stresses and mechanical surface treatments, current trends and future prospects, in: Proceedings of the Fourth International Conference on Residual Stresses, Society for Experimental mechanics Inc., Baltimore, MD, USA, 1994, pp. 1154–1163.

[5] N.R. Tao, M.L. Sui, J. Lu, K. Lu, Nanostruct. Mater. 11 (1999) 433–440.

[6] N.R. Tao, Z.B. Wang, W.P. Tong, M.L. Sui, J. Lu, K. Lu, Acta Mater. 50 (2002) 4416–4603.

[7] X. Wu, N. Tao, Y. Hong, B. Xu, J. Lu, K. Lu, Acta Mater. 50 (2002) 2075–2084.

[8] Y. Iwahashi, Y. Wang, J. Horita, M. Nemoto, T.G. Langdon, Acta Mater. 46 (1998) 3317–3331.

[9] G. Liu, J. Lu, K. Lu, Mater. Sci. Eng. A 286 (2000) 91–95.

[10] P.G. Sanders, J.A. Eastman, J.R. Weertman, Acta Mater. 45 (1997) 4019–4025.

[11] H.S. Yang, G.R. Bai, L.J. Thompson, J.A. Eastman, Acta Mater. 50 (2002) 2309–2317.

[12] L. Zhou, G.Q. Xu, S.F.Y. Li, P.K.H. Ho, P.C. Zhang, K.D. Ye, W.J. Wang, Y.F. Lu, Appl. Surf. Sci. 120 (1997) 149–158.

[13] G.B.M. Fiege, V. Feige, J.C.H. Phang, M. Maywald, S. Görlich, L.J. Balk, Microelectron. Reliability 38 (1998) 957–961.

[14] F. Ruiz, W.D. Sun, F.H. Pollak, Appl. Phys. Lett. 13 (73) (1998) 1802–1804.

[15] A.I. Buzin, P. Kamasa, M. Pyda, B. Wunderlich, Thermochim. Acta 381 (2002) 9–18.

[16] G.B.M. Fiege, A. Altes, R. Heiderhoff, L.J. Balk, J. Phys. D: Appl. Phys. 32 (1999) L13–L17.

[17] G.B.M. Fiege, F.-J. Niedernostheide, H.-J. Schulze, R. Barthelmeß, L.J. Balk, Microelectron. Reliability 39 (1999) 1149–1152.

[18] D.M. Price, M. Reading, A. Hammiche, H.M. Pollock, Int. J. Pharm. 192 (1999) 85–92.

[19] R.B. Dinwiddle, R.J. Pylkki, P.E. West, Thermal conductivity contrast imaging with a scanning thermal microscope, in: T.W. Tong (Ed.), Thermal Conductivity, vol. 22, Technomic Publishing Co., Lancaster, 1994, pp. 668–677.

[20] S. Gomes, N. Trannoy, P. Grossel, Meas. Sci. Technol. 10 (1999) 805–811.

[21] S. Gomes, N. Trannoy, Ph. Grossel, F. Depasse, C. Bainier, D. Charraut, Int. J. Therm. Sci. 40 (2001) 949–958.

[22] A. Hammiche, M. Reading, H.M. Pollock, M. Song, D.J. Hourston, Rev. Sci. Instrum. 67 (1996) 4268–4274.

[23] L. Zhou, G.O. Xu, H.T. Ng, S.F.Y. Li, J. Vac. Sci. Technol. B 15 (1997) 1871–1875.

[24] J.M. Dorlot, J.P. Baïlon, J. Masounave, Des matériaux, Deuxième édition revue et augmentée. Editions de l'Ecole Polytechnique de Montréal, Québec, Canada, 1999.

[25] H. Hoffmann, J. Vancea, Thin Solid Films 85 (1981) 147–167.

[26] K. Lu, Y.H. Zhao, Nanostruct. Mater. 12 (1999) 559–562.

[27] A.L. Geiger, D.P.H. Hasselman, P. Welch, Acta Mater. 45 (1997) 3911–3914.

[28] A. Goldsmith, T.E. Waterman, H.J. Hirschhorn, Elements, in: Handbook of Thermophysical Properties of Solid Materials, Revised Edition, vol. 1, Macmillan, New York, 1961.